Astron. Astrophys. 343, 983–989 (1999)

ASTRONOMY AND ASTROPHYSICS

Height variation of the solar granulation

J. Krieg, M. Wunnenberg, F. Kneer, M. Koschinsky, and C. Ritter

Universitäts-Sternwarte Göttingen, Geismarlandstrasse 11, D-37083 Göttingen, Germany

Received 29 October 1998 / Accepted 22 December 1998

Abstract. We analyze spectral scans of narrow-band images across the Na D_2 line. They were obtained from disc centre of the Sun with our Fabry-Perot interferometer (FPI) in the Vacuum Tower Telescope at the Observatorio del Teide. The FPI was set to a bandwidth of 200 mÅ FWHM and the spectral stepwidth was 100 mÅ. Our aim is to study the variation of the granulation pattern with height in the atmosphere. To achieve high spatial resolution the simultaneously taken broad-band images are restored with speckle methods. With the knowledge of these reconstructed images we were also able to restore the narrow-band images. The formation heights are found from *temperature response functions* $RF_{\rm T}$. In the wings of NaD_2, the response functions for different wavelengths exhibit a substantial overlap in atmospheric heights. Therefore we use linear combinations which allow a better height discrimination. Applying the same combinations to the D_2 images we can visualize the height variation of the granular pattern. The granular intensity fluctuations are a matter of the deep photosphere alone. They disappear at heights of about 100 km (above $\tau_{5000} = 1$).

Key words: techniques: image processing – techniques: spectroscopic – Sun: granulation – Sun: photosphere

1. Introduction

Dynamic phenomena on the Sun take place in three spatial dimensions. It is thus of interest to follow the processes, apart from their horizontal evolution, also along the height co-ordinate in the solar atmosphere. The present investigation deals with the variation of the granulation pattern with height in the atmosphere. This gives information on the penetration of the convective overshoot into the stably stratified photosphere.

Rodríguez Hidalgo et al. (1992) and Wilken et al. (1997, see also references in these papers), among others, used the centre-to-limb variation of high resolution images to study the height dependence of the granular phenomenon. The latter authors found, on the one hand, that the coarse granular structure fades away towards the limb. On the other hand, small-scale brightenings, presumably the bright rims of granules (de Boer et al. 1992), are still seen close to the limb, thus at larger heights in the atmosphere. Wilken et al. (1997) concluded that this observation favours the model calculations of granulation by Steffen et al. (1994) in which the bright rims are caused by penetration of hot material due to local underpressure.

Observations of the granular dynamics with slit-spectrographs (see e.g. Kneer et al. 1980, Durrant & Nesis 1982, Nesis et al. 1999, Nesis 1985, Komm et al. 1990, 1991a, 1991b, among many others) allow us to probe many atmospheric heights simultaneously by means of various formation heights of different spectroscopic features, albeit only along one horizontal co-ordinate. One conclusion with regard to the granular intensity fluctuations of many of the above studies is that the granular pattern reaches heights of only 150 km (above $\tau_{5000} = 1$). Higher up secondary processes are excited.

In the present paper we combine two-dimensional, high spatial resolution imaging with spectroscopy by means of a Fabry-Perot interferometer (FPI). At present, this still asks for rather involved image restoration. Therefore, we concentrate here on the outline of the methods and on images of the granulation taken in the wings of a strong Fraunhofer line. The results will enable us to directly see the granulation at different atmospheric heights and to follow, in two-dimensional images, its disappearance. The following Sect. 2 describes the instrumental setup and the observations and Sect. 3 the data analysis. We discuss *temperature response functions* in Sect. 4, in order to associate the images to certain "formation heights". Sect. 5 discusses the results and Sect. 6 concludes the paper with an outlook.

2. Observations

The observations were obtained in June 1997 with the Vacuum Tower Telescope (VTT) at the Observatorio del Teide. The data analyzed here stem from disc centre of the Sun. Two single spectral scans across Na D_2 with our FPI were selected. They are part of time sequences taken at different days. The data from two different days are chosen on purpose, to convince ourselves that the results are not singular in the sense that they are obtained from a special area on the Sun under special seeing conditions. The full analysis of the time sequences is laborious and is deferred to a subsequent contribution. The D_2 line was chosen despite its blended core since it has stronger wings than D_1, thus a stronger wavelength dependence of the height of formation of the wing intensities.

The FPI is described in Bendlin et al. (1992), Bendlin (1993), and Bendlin & Volkmer (1995). Referring especially to Fig. 3

Send offprint requests to: J. Krieg (jkrieg@uni-sw.gwdg.de)

in Bendlin et al. (1992) we comment here on its basic features and mention the changes from its normal setup: The telescope's primary focal plane (at F) is imaged into a plane at F′ in an optical laboratory of the VTT. In front of F′, a beam splitter takes out approximately 5% of the light which go into the broad-band channel. The remainder of the light goes straight into the narrow-band channel.

Broad-band channel. Here, an interference filter of 10 Å centred at Na D_2 and a variable grey filter are followed by a CCD – we call it CCD1 - located in a plane congruent to F′.

Narrow-band channel. The focal plane F′ is re-imaged onto F″ where another detector, CCD2, is mounted. The re-imaging is done in such a way that the FPI with its limited aperture can be placed at the image of the telescope's pupil. This position of the FPI gives a wavelength variation of the transmission (cf. Airy's formula) from the centre of the field of view to its corners. We neglect this in the data reduction for the present purposes since it amounts only to -16 mÅ in the raw images, and even less, -9 mÅ, in the remaining field of view after the restorations. The spacing of the FPI etalons was chosen to give 200 mÅ bandwidth (FWHM). Its finesse was approximately 35. To sort the orders of the FPI an interference filter with 3 Å FWHM, again centred at Na D_2, was placed close to F′. This is different from the setup described in Bendlin et al. (1992) where a universal birefringent filter (UBF) with low transmissivity ($\leq 10\%$) was used. (Actually, for regular use with high transmissivity ($> 50\%$), a second FPI is now mounted instead of the UBF close to the first one.)

An image scale of 0.″1 per pixel on the 384×286 Thomson chips of the slow-scan CCDs from LaVision was chosen. The simultaneous exposures of CCD1 and CCD2, the data transfer, and the variation of the spacing of the FPI etalons (to change the wavelength position of the passband) is done by computer control.

The scans across Na D_2 consisted of 140 short exposure (6 ms) frames taken with both CCD1 and CCD2. After each 5 exposures the FPI transmission was shifted by 100 mÅ so that we have 28 wavelength positions around Na D_2 in the narrow-band channel. Fig. 1 shows which intensities, relative to the quiet Sun continuum intensity, must be expected from the setup. The measured average frame intensities come close to the solid profile in Fig. 1.

In addition, several data were taken for the reduction later on: darks, flat fields (with defocussed telescope), scans with a fixed pattern in the VTT's primary focus to correct for relative displacements and slightly different scales of the images taken with CCD1 and CCD2.

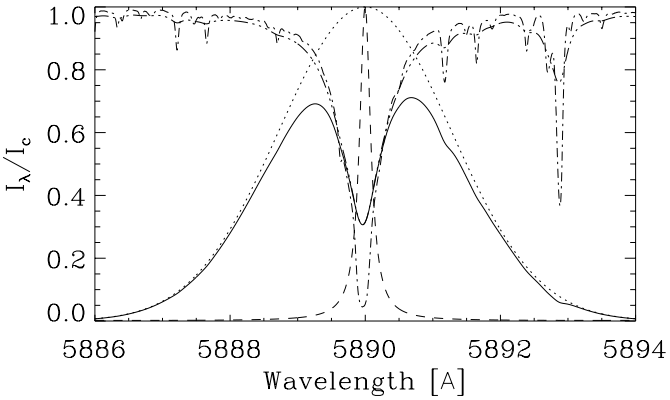

Fig. 1. Disc centre Na D_2 profiles. Dash-dotted: obtained with a Fourier Transform Spectrometer by Brault & Neckel (1987); dot-dot-dot-dashed: after convolution with the (normalized) FPI transmission curve (dashed, Airy's formula); solid: after multiplication of the convolved profile with a Gaussian (dotted) of 3 Å FWHM to mimic the order sorting interference filter.

3. Data analysis and image restoration

3.1. Pre-reduction

The usual corrections were applied: The average dark frames were subtracted. The gain tables of the CCDs were obtained from the average flat fields. The single frames were then divided by their appertaining gain tables (with respect to CCD1 and CCD2 and wavelength position for the latter). Treating single flat field frames as regular data gives information on the noise to be used below for the optimum filters. The images were corrected for the above mentioned displacements and differences of scales. Image motion was taken out by choosing the CCD1 (broad-band) frame with highest contrast and correlating the remaining 139 frames to the former. The same displacements were applied to the corresponding simultaneously taken CCD2 (narrow-band) frames. For further image restoration, i.e. removal of seeing (and telescope aberrations) within isoplanatic patches, the frames were divided into 48 partly overlapping subfields of 64×64 pixel each ($\hat{=}6.''4 \times 6.''4$). At the end, these subfields were recombined again to a full image.

3.2. Speckle reconstruction

For both scans analyzed here, the 140 frames from the broad-band channel (CCD1) were restored by speckle techniques, which are well established (cf. de Boer et al. 1992, de Boer & Kneer 1992, de Boer 1996, Wilken et al. 1997). We commonly use the spectral ratio method (von der Lühe 1984) to obtain the amplitude correction factors (in Fourier space) as well as the speckle masking method (Weigelt 1977, Weigelt & Wirnitzer 1983, Lohmann et al. 1983) to determine the phases with high reliability. Since the broad-band channel provides much light with high SNR we obtain reliable reconstructions with only 140 frames.

3.3. Restoration of narrow-band images

Given the reconstructed estimate of the object $\hat{o}_\mathrm{b}$ seen through the broad-band channel, the observed broad-band images $i_{\mathrm{b},l}$ at time l, and the appertaining narrow-band images $i_{\mathrm{n},l}$, we may perform a further image restoration and estimate the object $\hat{o}_{\mathrm{n},\lambda}$ at wavelength position λ in the narrow-band channel. The $\hat{}$ denotes estimates. Since the two channels operate in the same wavelength range we assume that their instantaneous point

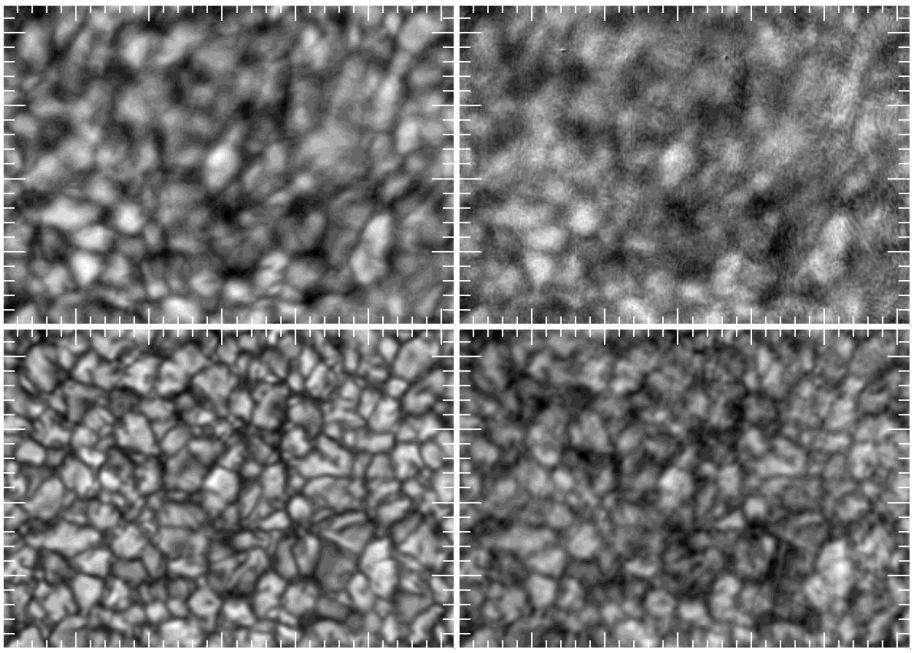

Fig. 2. Improvement of spatial resolution by image restoration. Upper images: simultaneously taken single frames from CCD1 (*left*) and CCD2 (*right*); lower images: speckle reconstruction (*left*) and image in the wing of D_2 (*right*) after restoration according to Eq. (5). The distance of the tickmarks is $1''$.

spread functions s_l are identical. Presumably, they are "broader" for the narrow-band channel compared to the broad-band channel due to more optical components in the former. Yet this is of no concern here, the assumption underestimates the corrections of the narrow-band images. Their spatial resolution is mainly limited by photon noise.

Denoting the Fourier transforms of the images and of the point spread functions by upper case letters, we obtain in Fourier space the relations, within an isoplanatic patch,

$$I_{\mathrm{b},l} = \hat{O}_{\mathrm{b}} S_l \tag{1}$$

and

$$I_{\mathrm{n},l} = \hat{O}_{\mathrm{n}} S_l \,, \tag{2}$$

or

$$I_{\mathrm{n},l} S_l^* = \hat{O}_{\mathrm{n}} |S_l|^2 \,, \tag{3}$$

where the '*' denotes the complex conjugate. Summing over all available l, here 5 at each wavelength position, gives

$$\hat{O}_{\mathrm{n}} = \frac{\sum_l I_{\mathrm{n},l} S_l^*}{\sum_l |S_l|^2} \,. \tag{4}$$

Compared to a summation of Eq. (3), the formulation of Eq. (4) avoids to a large extent divisions by very small numbers at Fourier co-ordinates where a single S_l becomes 0, i.e. the information is efficiently lost at this instant and wavenumber (cf. also Keller & von der Lühe 1992). Replacing now S_l by means of Eq. (1) and applying an optimum filter H (Brault & White 1971) yields finally

$$\hat{O}_{\mathrm{n}} = H \frac{\sum_l I_{\mathrm{n},l} I_{\mathrm{b},l}^*}{\sum_l |I_{\mathrm{b},l}|^2} \hat{O}_{\mathrm{b}} \,. \tag{5}$$

For the construction of the optimum filter we assume that the noise in the broad-band frames is negligible. In the same manner as Löfdahl (1996) we obtain

$$H = 1 - \left\langle |N|^2 \right\rangle \left\langle \frac{\sum_l |I_{\mathrm{b},l}|^2}{|\sum_l I_{\mathrm{n},l} I_{\mathrm{b},l}|^2} \right\rangle \,. \tag{6}$$

The averages $\langle \cdot \rangle$ on the right hand side are obtained by smoothing over 5×5 pixels for the fraction and by taking additionally azimuthal and subframe averages of $|N|^2$. Spikes in H larger than 1.0 are cut to 1.0 and values < 0.2 are set to zero. The noise term $\left\langle |N|^2 \right\rangle$ is calculated from the flat field frames, as mentioned above, and the values in the numerator and denominator on the right hand side are taken from the data themselves.

We demonstrate in Fig. 2 the tremendous improvement of image quality by restoration. Similar results had been shown by Krieg et al. (1998).

Fig. 3 gives results from one spectral scan. The intensity fluctuations in the wings of Na D_2 are very similar to those seen in the speckle reconstruction. But one sees already here that the granular pattern fades away in the images close to the line centre.

Furthermore, to lower the influence of noise, we combine the data on both sides of Na D_2 at approximately the same (absolute) wavelength distance from line centre. This increases the number of observed images from 5 to 10 in the sums of Eq. (5) while at the same time the optimum filter H widens. Dopplershifts are of little concern since we will deal with the damping wings.

4. Temperature response functions

We aim at associating the intensity fluctuations at certain distances from D_2 line centre to certain heights in the solar atmosphere. We do this by means of temperature response functions $RF_{\mathrm{T}}(z, \lambda)$, in short RFs (Mein 1971, Beckers & Milkey 1975,

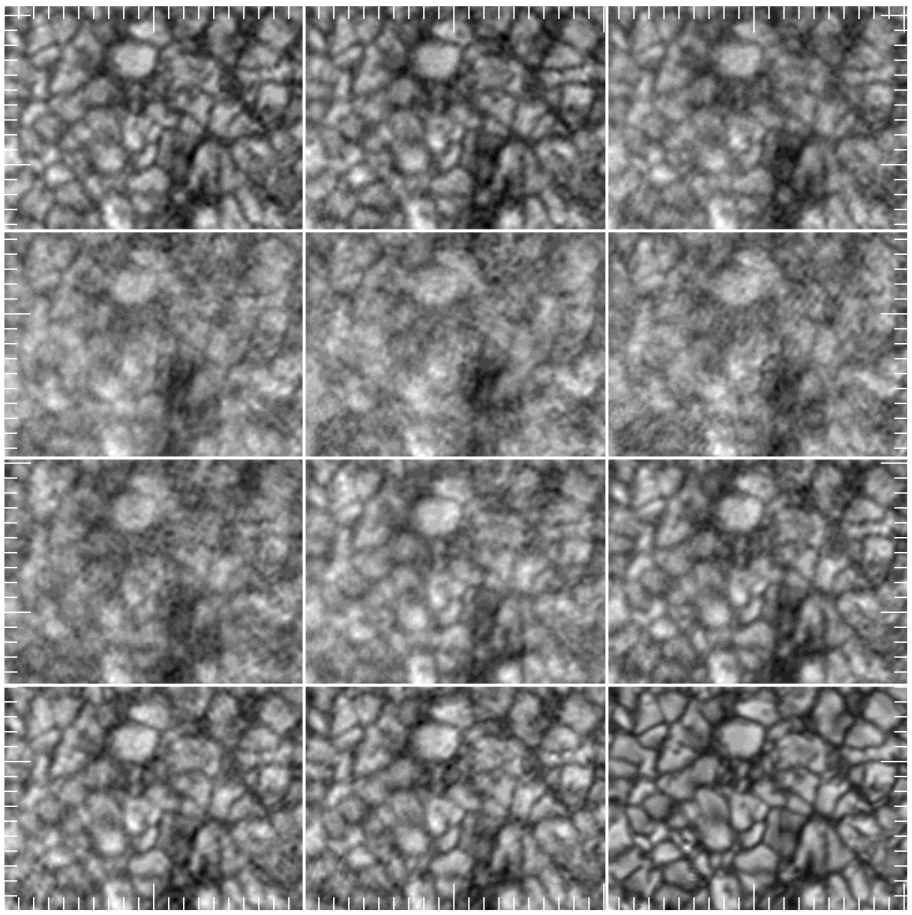

Fig. 3. $20'' \times 15''$ subfields of restored images from a FPI scan across Na D_2. The distance of the tickmarks is $1''$. The speckle reconstruction from the broad-band channel is shown in the lower right corner. The contrasts are scaled separately in each image to the local maximum and minimum. Starting in the upper left corner, moving to the right, and going down row by row, the wavelength displacements from Na D_2 line centre are (in Å): −1.18, −0.78, −0.48, −0.28, −0.08, +0.02 (approximately line centre, 2nd row right image), +0.12, +0.32, +0.52, +0.82, +1.22.

Caccin et al. 1977, Kneer et al. 1980). First, we calculate the intensity I_λ from the VAL C model atmosphere (Vernazza et al. 1981). The line parameters for D_2 and the sodium atomic parameters and abundance as in Kneer & Nolte (1994) are used. The calculations are done in LTE since we are exclusively interested in the wing intensities. This is justified from the calculations of e.g. Bruls et al. (1992). Next, we compute the intensity change $\delta I_{z,\lambda}$ if we change in the height range $[z, z+\delta z]$ the temperature by the factor $(1+\delta \mathrm{T}/\mathrm{T}(z))$. We define the temperature response function as

$$RF_\mathrm{T}(z,\lambda) = \frac{\delta I_{z,\lambda}}{I_\mathrm{c}} / (\delta z (\delta \mathrm{T}/\mathrm{T}(z))\,, \tag{7}$$

where I_c is the continuum intensity. In this way RF_T simply gives the reaction of the intensity to a temperature change at z.

We keep the pressure unchanged when modifying the temperature. It was shown by Kneer & Nolte (1994) that, for Na D_2, pressure fluctuations have a much smaller influence on the wing intensities than temperature fluctuations. We may savely take the intensity pattern in the wings as proxy for the temperature structure.

Fig. 4a depicts some response functions calculated in the above manner with $\delta \mathrm{T}/\mathrm{T} = 0.05$, which is small, i.e. in the linear regime of the reaction of I_λ to temperature changes. The minimum of $RF_\mathrm{T}(z)$ for the continuum (leftmost solid curve in Fig. 4a) is due to the negative contributions of the H^- opacity (cf. Kneer et al. 1980).

However, instead of using the RFs in Fig. 4a calculated for infinite spectral resolution and in order to mimic the actual resolution, we convolved $RF_\mathrm{T}(z,\lambda)$ also with Airy's FPI function for 200 mÅ FWHM at fixed z. We call the results $RF_{\mathrm{T,Airy}}(\Delta\lambda)$. Some are given in Fig. 4b, at line centre, at 250 mÅ and at 450 mÅ off line centre. All RFs span larger height ranges than those of Fig. 4a. Besides, the speckle reconstructed image was obtained through a 10 Å FWHM filter centred at D_2. Since we do not have the actual transmission curve we approximate the contributions of intensities within the filter pass-band to the fluctuations by averaging $RF_\mathrm{T}(z,\lambda)$ for fixed z over 8 Å. The effect is also shown in Fig. 4b. One notices the difference between the dotted curve, the pure continuum RF, and the solid curve, the averaged RF, which we denote by $RF_{\mathrm{T,a}}$. The latter has more contributions from higher atmospheric layers. A number which will be needed later is the intensity I_a averaged over 8 Å relative to the continuum intensity: $I_\mathrm{a}/I_\mathrm{c} \approx 0.87$.

The RFs in Fig. 4b possess a substantial overlap of contributing atmospheric heights. We can reduce this by using linear combinations of the RFs in Fig. 4b. Suitable combinations are found by estimates and the restriction that the RF be not too negative. Some are shown in Fig. 4c: solid curve (1a): $RF_{\mathrm{T,a}} - 0.30 RF_{\mathrm{T,Airy}}(450m\text{Å})$; long-dashed (1b): $RF_{\mathrm{T,a}} - 0.30 RF_{\mathrm{T,Airy}}(250m\text{Å})$; short-

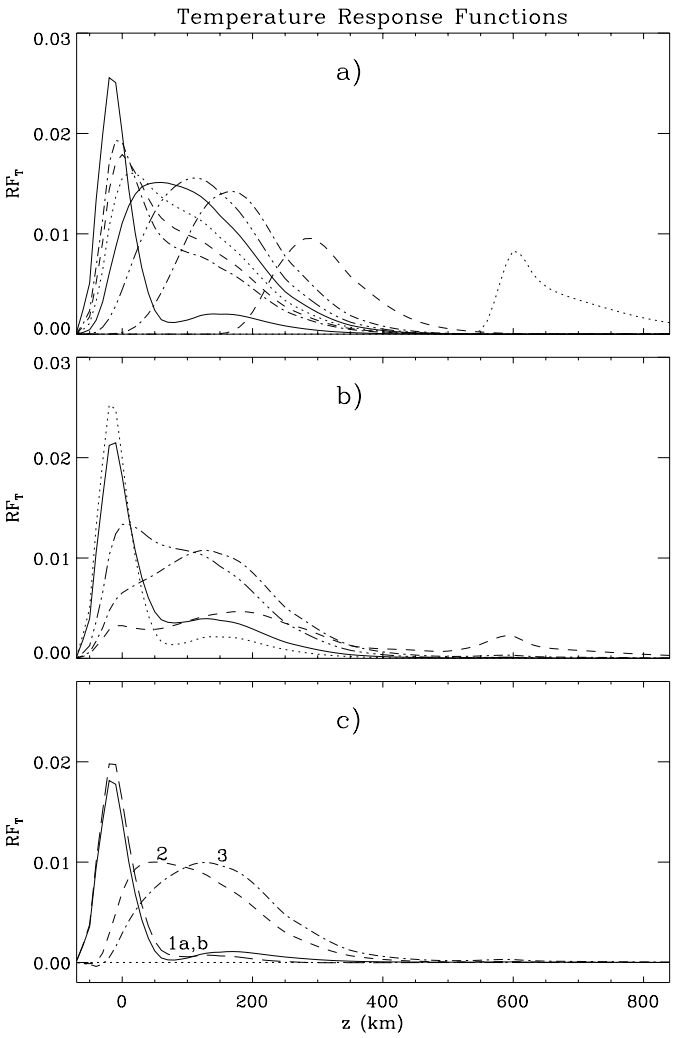

Fig. 4a–c. Temperature response functions $RF_{\rm T}(z,\lambda)$ in units of $(\delta I_\lambda/I_{\rm c})\,{\rm km}^{-1}(\delta{\rm T}/{\rm T})^{-1}$; **a** with infinite spectral resolution at distances $\Delta\lambda$ from line centre (in mÅ, from *right* to *left*): 0, 100, 200,..., 700, and continuum (solid leftmost curve); **b** dotted: continuum as in **a**; solid: after averaging over an 8 Å wavelength band centred at D_2; other curves: response functions after convolution with Airy's FPI function of 200 mÅ FWHM at line centre (dashed), at 250 mÅ (dot-dashed) and at 450 mÅ off line centre (dot-dot-dot-dashed); **c** linear combinations of response functions in **b**, see text for details.

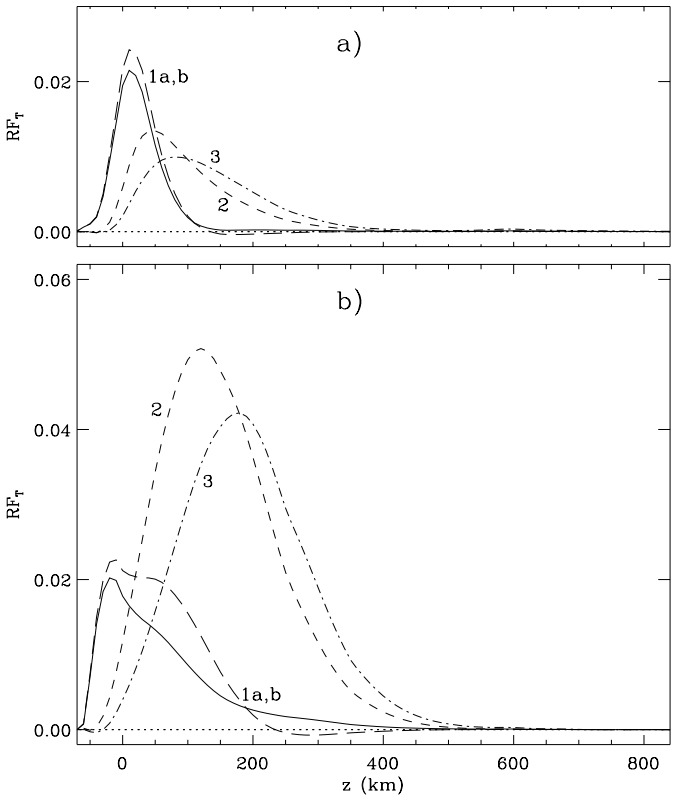

Fig. 5a and b. Temperature response functions $RF_{\rm T}(z,\lambda)$ after the same treatment leading to the RFs of Fig. 4c; **a** δT/T(z) = +0.25; **b** $\delta{\rm T}/{\rm T}(z) = -0.25$.

dashed (2): $RF_{\rm T,Airy}(450m\text{Å}) - 0.35RF_{\rm T,a}$; dot-dashed (3): $RF_{\rm T,Airy}(250m\text{Å}) - 0.20RF_{\rm T,a}$.

We can now better discriminate between various formation heights of intensity fluctuations. The centres of gravity of the RFs 1a, 1b, 2, and 3 approximately are at heights of -10 km (without the tail above 70 km), 0 km, 125 km, and 165 km, respectively.

We must not expect that the temperature fluctuations are small, ≈5% at fixed heights. To study the non-linearity of the D_2 wing intensities we calculated RFs with δT/T = $\pm$0.25. We restrict the discussion to the linear combinations as in Fig. 4c. They are presented in Fig. 5a for δT/T = +0.25 and in Fig. 5b for $\delta{\rm T}/{\rm T} = -0.25$, with the same coding as in Fig. 4c. Although the general behaviour of the RFs is similar to those of Fig. 4c, we notice the strong temperature dependence of the D_2 wing intensities: Large temperature enhancements increase very much the ionization of sodium and weaken the wing strength of D_2. In that case, the RFs of the wings move to somewhat lower heights compared to those of Fig. 4c. On the other hand, strong temperature reductions lead to highly increased neutral sodium densities and to increased wing strengths. In that case, low wing intensities are "formed" in high atmospheric layers. The wavelength integrated image, (and linear combinations of it with wing images) is less dramatically influenced by temperature decreases.

5. Results and discussion

We are now close to the point where we can relate the restored images to heights in the solar atmosphere. The RFs give intensity variations relative to the continuum intensity. Therefore we multiply the fluctuations in the images, which are relative to the mean intensity at each wavelength position, with the factor $I_\lambda/I_{\rm c}$ taken from the convolved D_2 profile (dot-dot-dot-dashed profile in Fig. 1) at the appertaining wavelength λ. Likewise, the speckle-reconstructed image fluctuations were multiplied with the above factor 0.87 resulting from the averaging over 8 Å about the Na D_2 line. Furthermore, for a linear combination of images, these have to be of the same image quality, i.e. they must possess the same spatial resolution. Thus, the speckle reconstructions

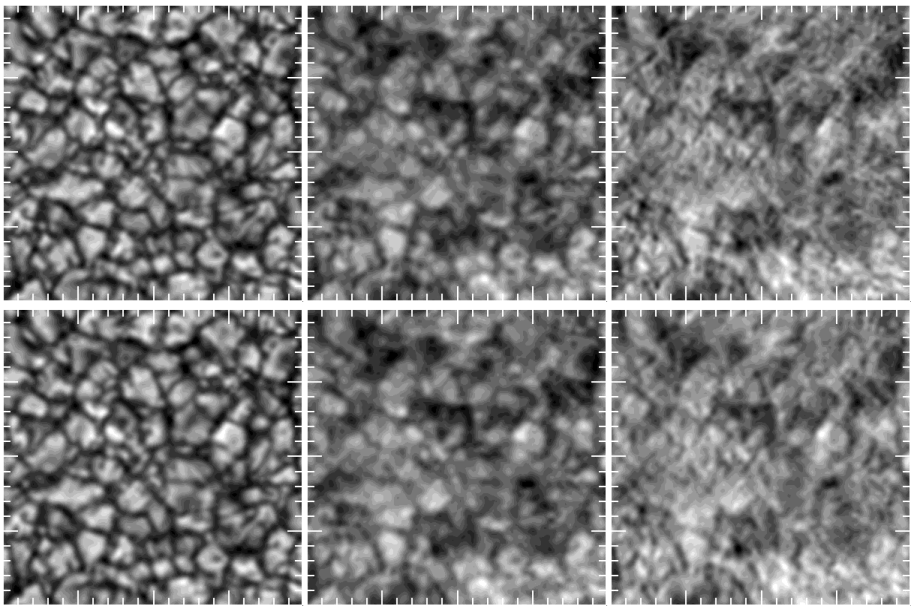

Fig. 6. $20'' \times 20''$ images from the deep photosphere (*leftmost*) and higher up (*rightmost*) constructed from the same spectral scans as the images of Fig. 2, according to the above prescription of linear combinations for 450 mÅ off line centre (*upper image*) and 250 mÅ (*lower image*). The middle two images are the restored images from the wings. Distance of tickmarks: $1''$.

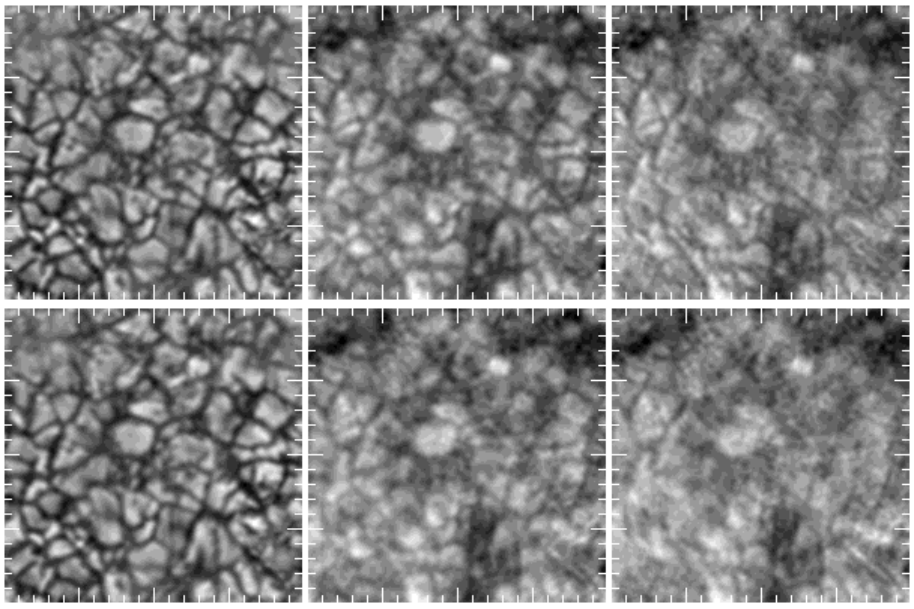

Fig. 7. $20'' \times 20''$ images from the same spectral scan as Fig. 3; linear combinations as in Fig. 6 but calculated for 500 mÅ off line centre (*upper row*) and for 300 mÅ (*lower row*). Distance of tickmarks: $1''$.

were treated locally (in each sub-image) with the same filter H as the D_2 wing images with which they are to be combined. And finally, the linear combinations of images according to the prescriptions in the previous section were built: We calculated, pixel by pixel, new intensities with the same linear combinations as for the response functions in Fig. 4c. For instance, we calculate a new image $I_{\rm new} = I(450m\text{Å}) - 0.35I(integrated\ light)$.

Fig. 6, now, shows in two rows a $20'' \times 20''$ section of Fig. 2 treated in the above manner at 450 mÅ and 250 mÅ off line centre, respectively. The left images give the granular pattern as it is seen from the deep photosphere. In Fig. 4c, the RFs 1a (solid) and 1b (long-dashed) correspond to the upper and lower left images of Fig. 6, respectively. Comparing these with the speckle reconstruction of Fig. 2 one certainly notices the decrease of spatial resolution due to the filtering necessary for the linear combinations. But most of the features are still present. The middle images in Fig. 6 are the direct reconstructions of the wing observations at the above wavelengths. Here, the granulation is still shining through, more at 450 mÅ off line centre than at 250 mÅ. The right images are the linear combinations according to the recipe of the previous section. The granular pattern has essentially disappeared. Only with the knowledge of the left images one can recognize few low-contrast, granular structures, less clearly at 250 mÅ off line centre (lower image) than at 450 mÅ (upper image). In other words, in view of the curves 1a, 1b, 2, and 3 of Fig. 4c, granular *intensity* fluctuations are a matter of the deep photosphere alone. This agree with the result by Espagnet et al. (1995).

Fig. 7 shows the result from the other spectral scan, the same as in Fig. 3, and for 500 mÅ and 300 mÅ off line centre. It is

again clearly seen that the granular intensity fluctuations disappear rapidly with height in the atmosphere.

At some places very dark features occur in the images from the high atmosphere. In most cases, they are related to intergranular spaces. Referring to Fig. 5b we conjecture that these are formed higher than average. These dark features may thus extend over heights of 200–300 km in the photosphere. The bright borders of granules (de Boer et al. 1992) may also be seen in high layers. But generally this is not the case. Considering the overlap of the RFs in Fig. 5a (for $\delta T/T = +0.25$), we cannot decide from this analysis whether the corresponding temperature enhancements are bound to the deep photosphere or whether they penetrate to layers of 100 km or more. Still better separated RFs are needed (or combinations of them) together with low noise data amenable to more refined linear combinations. In any case, there is no indication of an *anti-correlation* of intensities formed in the deep photosphere and in higher layers. The anti-correlation was expected in early models of the granular overshoot into stably stratified atmospheric layers (see e.g. Holweger & Kneer 1989 and references there).

6. Conclusion and outlook

Two-dimensional imaging of the Sun with high spatial resolution was possible already for some time. High spectral resolution together with high spatial resolution is becoming feasible. Here we have analyzed narrow-band images in the wings of the Na D_2 line with the aim at studying the variation of the granular temperature structure with atmospheric height. We have presented ways of image restoration which lead to a substantial increase of information on small-scale structures seen in narrow wavelength bands. Using linear combinations of high resolution images, to better discriminate between formation heights, we could visualize the disappearance of the granulation with increasing height. This confirms earlier results by Kneer et al. (1980, see also Nesis 1985 and references there) as well as Espagnet et al. (1995). We could not see any anti-correlation between intensity fluctuations formed in deep and higher layers.

We will continue analysing the time sequences from which the present data sets are taken. The method of two-dimensional spectroscopy with image restoration will then develop its full advantage over spectroscopy with conventional slit-spectrographs in studying small-scale processes in the solar atmosphere. While the intensity pattern formed in high layers ($\approx$150 km) appears to have no ordered structure, this may be different when following their temporal evolution. Also, preliminary Dopplergrams with high spatial resolution, obtained from differences of images in the blue and red flank of Na D_2, show interesting small-scale features.

Restoration of narrow-band images gives new insight into the dynamic processes of the solar atmosphere. Yet, the smaller the bandwidth the larger is the photon noise. Thus, for high spatial, spectral, and temporal resolution large telescopes are needed.

Acknowledgements. Financial support by the *Deutsche Forschungsgemeinschaft* through grants KN 152/17-1,2 and KN 152/19-1,2 and by the *Graduiertenkolleg* "Strömungsinstabilitäten und Turbulenz" is gratefully acknowledged. The Vacuum Tower Telescope at the Spanish Observatorio del Teide of the Instituto de Astrofísica de Canarias/Tenerife is operated by the Kiepenheuer-Institut für Sonnenphysik in Freiburg, Germany.

References

Beckers J.M., Milkey R.W., 1975, Solar Phys. 443, 289
Bendlin C., Volkmer R., Kneer F., 1992, A&A 257, 817
Bendlin C., 1993, Ph.D. Thesis, Göttingen University
Bendlin C., Volkmer R., 1995, A&AS 112, 371
Brault J.W., Neckel H., 1987, Spectral Atlas of Solar Absolute Disk-averaged and Disk-center Intensities from 3290 to 12510 Å, unpublished
Brault J.W., White R.O., 1971, A&A 13, 169
Bruls J.H.M.J., Rutten R.J., Shchukina N.G., 1992, A&A 265, 237
Caccin B., Gomez M.T., Marmolino C., Severino G., 1977, A&A 54, 227
de Boer C.R., 1996, A&AS 120, 195
de Boer C.R., Kneer F., 1992, A&A 264, L24
de Boer C.R., Kneer F., Nesis A., 1992, A&A 257, L4
Durrant C.J., Nesis A., 1982, A&A 111, 272
Espagnet O., Muller R., Roudier Th., Mein N., Mein P., 1995, A&AS 109, 79
Holweger H., Kneer F., 1989, Spatially resolved spectra of solar granulation. In: Rutten R.J., Severino G. (eds.) Solar Granulation. NATO ASI Series C, Vol. 263, Kluwer Acad. Publishers, p. 173
Keller C., von der Lühe O., 1992, A&A 261, 321
Kneer F., Nolte U., 1994, A&A 286, 309
Kneer F., Mattig W., Nesis A., Werner W., 1980, Solar Phys. 68, 31
Komm R., Mattig W., Nesis A., 1990, A&A 239, 340
Komm R., Mattig W., Nesis A., 1991a, A&A 243, 251
Komm R., Mattig W., Nesis A., 1991b, A&A 252, 812
Krieg J., Kneer F., Koschinsky M., Ritter C., Starck J.-L., 1998, Ground-based observation with high spatial and spectral resolution. In: Harris R.H., Moreno Insertis F., Priest E. (eds.) A Crossroads for European Solar and Heliospheric Physics. ESA SP-417, p. 317
Löfdahl M.G., 1996, Ph.D. Thesis, Stockholm University
Lohmann A.W., Weigelt G.P., Wirnitzer B., 1983, Applied Optics 22, 4028
Mein P., 1971, Solar Phys. 20, 3
Nesis A., 1985, Ph.D. Thesis, Technische Universität Berlin
Nesis A., Hammer R., Kiefer M., et al., 1999, A&A, in press
Rodríguez Hidalgo I., Collados M., Vázquez M., 1992, A&A 254, 371
Steffen M., Freytag B., Holweger H., 1994, Shocks in the solar photosphere and their spectroscopic signature. In: Schüssler M., Schmidt W. (eds.) Solar Magnetic Fields. Cambridge Univ. Press, p. 298
Vernazza J.E., Avrett E.H., Loeser R., 1981, ApJS 45, 635
von der Lühe O., 1984, J. Opt. Soc. Am. A1, 510
Weigelt G.P., 1977, Optics Comm. 21, 55
Weigelt G.P., Wirnitzer b., 1983, Optics Letters 8, 389
Wilken V., de Boer C.R., Denker C., Kneer F., 1997, A&A 325, 819